PHYSICAL REVIEW B **84**, 134424 (2011)

Magnetic and thermal properties of $Er_{75}Dy_{25}$ single crystals

Mahmud Khan,[*,†] D. L. Schlagel, and T. A. Lograsso
The Ames Laboratory, US Department of Energy, Iowa State University, Ames, Iowa 50011-3020, USA

K. A. Gschneidner, Jr. and V. K. Pecharsky
The Ames Laboratory, US Department of Energy, Iowa State University, Ames, Iowa 50011-3020, USA, and Department of Materials Science and Engineering, Iowa State University, Ames, Iowa 50011-2300, USA

(Received 25 April 2011; revised manuscript received 16 June 2011; published 18 October 2011)

We report on an experimental study of the thermal and magnetic properties of $Er_{75}Dy_{25}$ single crystals with magnetic fields applied parallel to the [0001] and $[10\bar{1}0]$ directions. The [0001] direction is the easy axis of magnetization, while the $[10\bar{1}0]$ direction is the hard axis of magnetization. Three major transitions are observed in the heat capacity, magnetization, and alternating current magnetic susceptibility data. A first-order transition is observed at ~30 K, and two second-order transitions occur at ~45 and ~110 K. The *H-T* phase diagrams constructed from the experimental data reveal that several magnetic phases, including ferromagnetic cone, ferromagnetic fan, and *c* axis–modulated phases, exist in an $Er_{75}Dy_{25}$ single crystal. Both similarities and dissimilarities are observed in the *H-T* phase diagrams of $Er_{75}Dy_{25}$ when compared to the *H-T* phase diagrams of pure Er single crystals.

DOI: 10.1103/PhysRevB.84.134424 PACS number(s): 75.20.En, 75.30.Gw, 75.40.Cx, 75.50.Cc

I. INTRODUCTION

The lanthanide metals erbium (Er) and dysprosium (Dy) exhibit complex yet fascinating thermal and magnetic properties.[1–7] Both metals adopt hexagonal closed packed (hcp) crystal structure at room temperature,[6,8,9] and upon cooling down from room temperature, they both undergo a series of phase transitions where either or both magnetic and crystallographic sublattices are affected.[8]

Earlier investigations of Er performed using neutron and x-ray diffraction[1,10,11] show that an antiferromagnetic (AFM) transition occurs at $T_{N\parallel} \cong 84$ K (magnetization is parallel to the *c* axis), where paramagnetic (PM) compound orders in a *c* axis–modulated (CAM) structure. At $T_{N\perp} \cong 53$ K (magnetization is perpendicular to the *c* axis), another AFM transition takes place, during which the CAM structure changes to an antiphase domain (APD) cone plus helix structure. Upon further cooling, at ~25 K Er transforms into an alternating cone structure. The APD structure changes to a ferromagnetic (FM) cone along the *c* axis plus helix structure at $T_C \cong 19$ K. This FM transition is of the first order and is accompanied by a discontinuous 0.38% change in the lattice parameter *c*.[12] Synchrotron x-ray scattering study showed that Er also exhibits a sequence of lock-in transitions, which were explained by a spin slip model.[13] These spin slip transitions were also observed in the direct current (DC) magnetometry and alternating current (AC) susceptometry studies of single-crystal Er.[6]

Elemental Dy, which is PM at room temperature, also exhibits several magnetic field- and temperature-driven magnetic transitions.[7,14–16] Upon cooling down to the Neel temperature, $T_N \cong 180$ K, in a zero magnetic field, the PM Dy transforms into a helix AFM-ordered state. The AFM order changes over to the FM one below $T_C \cong 90$ K. When a magnetic field is applied anywhere between T_C and 135 K, the magnetic structure of Dy changes from a helix AFM to FM.[7,17] Between 135 and 180 K, the AFM-FM transition is separated by an intermediate fan magnetic phase, which is stable between ~7 and ~25 kOe.[7,17] Low-temperature x-ray diffraction studies of single-crystal Dy showed that the FM transition at 90 K is accompanied by a structural transition from hcp to a distorted orthorhombic structure, along with significant discontinuities in lattice parameters.[18–20] Below T_N, only a strong expansion of the *c* parameter is reported.

When two lanthanide metals are mixed, the magnetic and thermal properties of the resulting alloys may become interesting. Some such alloy systems that have been investigated include Tb-Er,[21,22] Nd-Dy,[23] and Er-Pr.[24–26] In the Er-Pr system, it was found that the addition of Pr significantly increases the heat capacity of Er, making the Er-Pr system suitable for cryocooler regenerator applications.[24,25] Multiple magnetic ordering transitions were recently discovered in pseudobinary $R_{1-x}R'_xAl_2$ alloys, where R and R' are rare earth metals with second-order Steven's factors of opposite sign.[27–30] Hence, mixing of two lanthanide metals can result in unusual behaviors not only in pseudobinary lanthanide metals but also in rare earth based intermetallic compounds.

Among the $R_{1-x}R'_xAl_2$ systems studied to date, the $Er_{1-x}Dy_xAl_2$ alloys exhibit the most pronounced first-order heat capacity peaks,[29] which is the key characteristic of the multiple magnetic ordering phenomenon mentioned earlier. Among the $Er_{1-x}Dy_xAl_2$ alloys, the alloy with $x = 0.25$ reveals the sharpest heat capacity anomaly. It is therefore interesting to explore the magnetic and thermal properties of pseudobinary Er-Dy lanthanide alloy, especially with 25% Dy. Here we report an experimental study of $Er_{75}Dy_{25}$ single crystals.

II. EXPERIMENTAL DETAILS

Single-crystal samples of $Er_{75}Dy_{25}$ were prepared from 99.8+ at.% (99.98 wt.%) pure (with respect to all other elements in the periodic table) Er and Dy by the Materials Preparation Center of the Ames Laboratory.[31] Appropriate quantities of the rare earth metals were arc melted together under an argon atmosphere several times and then dropcast into a copper chilled mold. The ingot was cold worked by hitting it with a ball-peen hammer and then heat treated for 10 days at 1400 °C. The resulting crystal was oriented by the back reflection Laue technique, and samples were cut from the oriented ingot by spark erosion. The faces were ground flat and parallel by standard metallographic techniques. Three samples (two for heat capacity measurements and one for magnetization measurements) were thus prepared. The specimen for the magnetization measurements was shaped as a parallelepiped, $1.37 \times 1.4 \times 0.99$ mm^3 in size. The specimens for the heat capacity measurements were bigger and measured $5 \times 5 \times 2$ mm^3, with the *b*- or *c*-crystallographic axis parallel to the shortest dimension.

A superconducting quantum interference device magnetometer MPMS XL-7 made by Quantum Design was used to collect the DC and AC magnetic data. The measurements were performed in the temperature range of 2–300 K and in applied magnetic fields of up to 7 T. The AC susceptibility measurements were performed in an AC field of $H_{\mathrm{ac}} = 5$ Oe and at frequencies ranging from 1 to 1000 Hz in zero and applied DC magnetic fields of 0 to 40 kOe. A homemade adiabatic heat-pulse calorimeter was used to conduct the heat capacity measurements.[32] The measurements were performed in the temperature range from ∼2 to 350 K in zero magnetic fields and in applied magnetic fields $\leqslant$15 kOe.

III. RESULTS AND DISCUSSION

A. Properties in the [0001] direction (or along the *c* axis)

The heat capacity C_P of single-crystalline $\mathrm{Er}_{75}\mathrm{Dy}_{25}$ measured in different magnetic fields applied parallel to the *c* axis is shown in Fig. 1(a). Three transitions are observed at ∼30, ∼45, and ∼110 K. The sharp peak at $T_C \cong 30$ K corresponds to the first-order AFM-FM transition. A similar transition (sharp peak) is observed in the C_P data of pure Er at $T_C \cong 19$ K.[33,34] In pure Dy, the first-order C_P peak is observed at $T_C \cong 90$ K.[3,7] The transition observed at ∼45 K resembles the anomaly observed in the C_P of pure Er at $T_{N\perp} \cong 53$ K, where the CAM structure transforms into the APD magnetic structure.[3,33] No such anomaly is observed in pure Dy. The anomaly at ∼110 K corresponds to the second-order AFM-PM transition and is similar to the anomalies observed in the heat capacities of pure Er and Dy at $T_{N\parallel} \cong 84$ K and $T_N \cong 180$ K, respectively. The spin slip transitions observed in pure Er[34] are not observed in the C_P of the $\mathrm{Er}_{75}\mathrm{Dy}_{25}$ single crystal.

The first-order peak at ∼30 K is strongly suppressed by the magnetic field, and it completely disappears when a magnetic field of 15 kOe is applied. A similar behavior is observed in pure Er, where application of the magnetic field suppresses the first-order peak.[34] The 45 K anomaly shifts to lower temperatures and vanishes as the magnetic field is increased. The anomaly at 110 K remains practically unaffected by these magnetic fields. As Dy is mixed with Er, T_C and $T_{N\parallel}$ increase nearly linearly (Fig. 1(b), where the data points for pure Er and Dy are taken from Refs. 3 and 33). This increase correlates with the magnitude of the de Gennes factor of Dy^{3+} (7.08), which is higher than that of Er^{3+} (2.55). On the contrary, $T_{N\perp}$ decreases upon adding Dy.

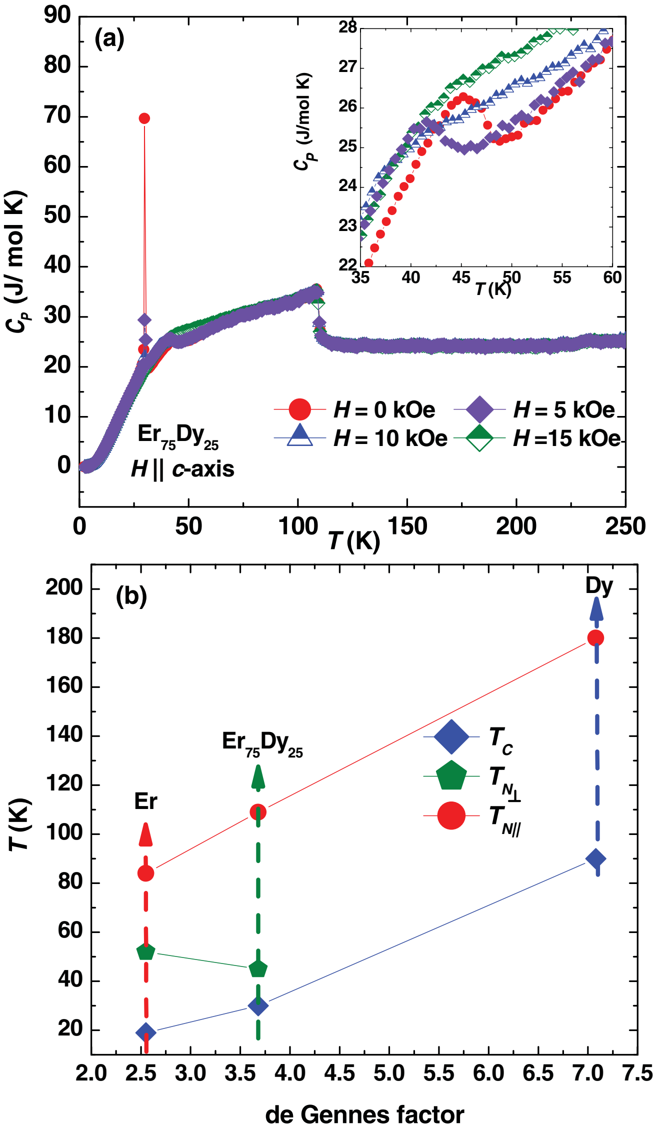

FIG. 1. (Color online) (a) The heat capacities of the $\mathrm{Er}_{75}\mathrm{Dy}_{25}$ single crystal measured in different magnetic fields applied along the *c* axis. The inset clarifies the behavior around the 45 K anomaly. (b) The different transition temperatures, observed in pure Er, $\mathrm{Er}_{75}\mathrm{Dy}_{25}$, and pure Dy as a function of Dy concentration.

The temperature dependencies of DC magnetization, $M(T)$, measured under zero field–cooled (ZFC) warming, field-cooled cooling (FCC), and field-cooled warming (FCW) conditions in magnetic field of 100 Oe applied along the *c* axis are shown in Fig. 2. The inset of Fig. 2 shows the derivative of the $M(T)$ data, and from these data the temperatures of different transitions observed in the $M(T)$ data are obtained. The first-order transition is observed at ∼31 K on heating and ∼28 K on cooling. A second-order APD-CAM transition is observed at ∼45 K on both heating and cooling. The second-order CAM-PM transition observed at ∼110 K in the C_P of $\mathrm{Er}_{75}\mathrm{Dy}_{25}$ is barely visible in the $M(T)$ data of Fig. 2; as shown in the inset of Fig. 2, a weak anomaly is observed in the derivative of the $M(T)$ data at ∼110 K. The APD-CAM and CAM-PM transitions mentioned previously are assumed based on the similarities between the experimental observations for pure Er (e.g., see Refs. 5 and 6) and those for $\mathrm{Er}_{75}\mathrm{Dy}_{25}$ (current work). The 84 K transition in pure Er is also barely visible in

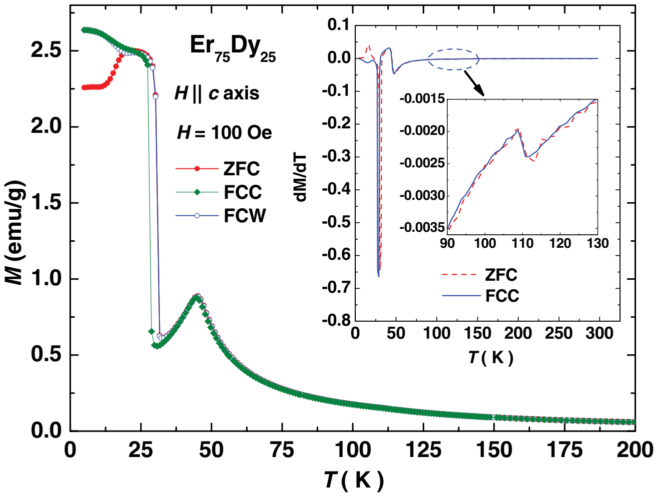

FIG. 2. (Color online) The temperature dependencies of the DC magnetization of $Er_{75}Dy_{25}$ measured in a 100 Oe magnetic field applied along the c axis under ZFC, FCC, and FCW conditions. The inset shows the derivatives of the ZFC and FCC data.

the $M(T)$ data.[6] The spin slip transitions that are observed in the $M(T)$ data along the c axis of the Er single crystal (see Ref. 6) are not observed in the $M(T)$ data along the c axis of the $Er_{75}Dy_{25}$ single crystal.

Figure 3 shows the $M(T)$ data of $Er_{75}Dy_{25}$ measured along the c axis on heating at different magnetic fields ranging from 10 to 50 kOe in 10 kOe increments. The only transition observed in each data set is the first-order transition at T_C, temperature of which increases linearly with increasing magnetic field. The APD-CAM transition, seen in the 100 Oe $M(T)$ data at ∼45 K, is not observed in any of the $M(T)$ data shown in Fig. 3. The anomaly at ∼110 K (Fig. 3 inset) is more pronounced in the high magnetic field $M(T)$ data.

The isothermal magnetization, $M(H)$, data of $Er_{75}Dy_{25}$ along the c axis measured at 2 and 5 K are shown in Fig. 4. The 2 and 5 K data show insignificant differences, and typical FM behavior is observed at both temperatures, suggesting that the easy magnetization direction of $Er_{75}Dy_{25}$ is along the c axis, which is consistent with the easy axis of magnetization of pure Er being the c axis.[35] The magnetic moment at 70 kOe is 243 emu/g (7.23 μ_B/f.u.), which is less than the expected theoretical value of 9.25 μ_B. This suggests that similar to pure Er, the $Er_{75}Dy_{25}$ alloy is a cone with a nonzero angle between the magnetic moment and the c axis. The upper inset of Fig. 4 shows the $M(H)$ data at temperatures ranging from 23 to 65 K along the c axis. The data show the transformation of the magnetic structure from the FM to the PM type with increasing temperature. The lower inset of Fig. 4 points to a weak metamagnetic behavior at ∼5 kOe in the vicinity of 40 K. This correlates well with the transition observed at ∼42 K in the 100 Oe $M(T)$ data and with the disappearance of this transition at higher magnetic fields (see Figs. 2 and 3).

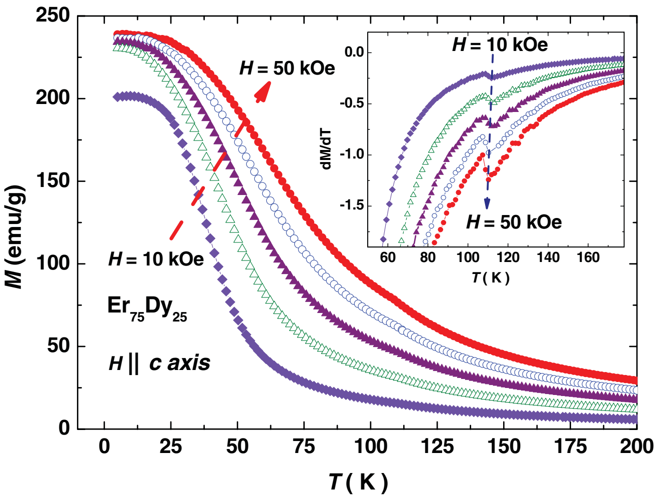

FIG. 3. (Color online) The $M(T)$ of $Er_{75}Dy_{25}$ measured in applied magnetic fields from 10 to 50 kOe in 10 kOe increments applied along the c axis. The inset shows the derivatives of the data obtained at each field.

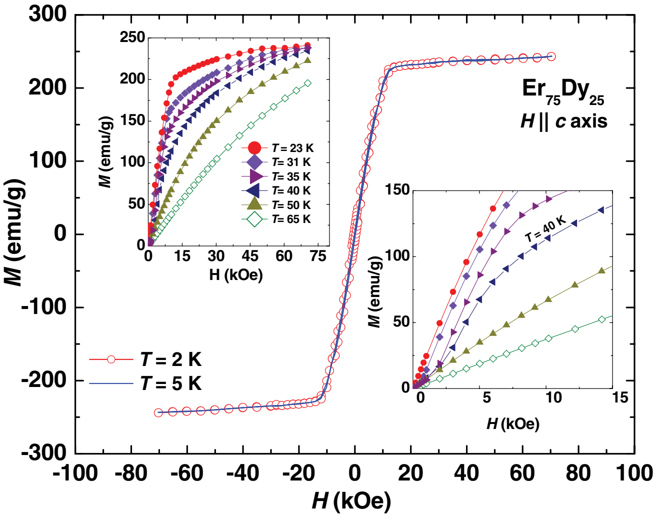

FIG. 4. (Color online) The field dependence of magnetization along the c axis of $Er_{75}Dy_{25}$ measured at 2 and 5 K. The upper inset shows the field dependence of magnetization of the same measured at higher temperatures. The lower inset shows the low field behavior of the magnetization data shown in the upper inset.

The temperature dependence of the real component of AC susceptibility, $\chi'(T)$, of $Er_{75}Dy_{25}$ measured along the c axis in zero DC magnetic fields is shown in Fig. 5 (a). The measurements were performed on heating in an AC field (H_{ac}) of 5 Oe at different frequencies. The $\chi'(T)$ data exhibit a sharp peak at ∼30 K due to the first-order transition from the FM to the APD state, and a broader peak at ∼45 K due to the second-order APD-CAM transition. As shown in the upper inset of Fig. 5(a), below ∼31 K, the $\chi'(T)$ data are frequency dependent: with increasing frequency, the magnitude of χ' below T_C decreases, showing that the alloy becomes less responsive to the AC field. The sharp peak at T_C also tends to diminish with increasing frequency. The derivative of the χ' data shows a third transition at ∼110 K, which is similar to the behaviors observed in Figs. 2 and 3, where the transition at 110 K is only observed in the derivative of the $M(T)$ data.

Figure 5 (b) shows the $\chi'(T)$ data of $Er_{75}Dy_{25}$ measured in the 0 and 5 kOe magnetic fields applied along the c axis of the crystal. Consistent with the behavior observed in the C_P data (see Fig. 1(a)), the peak at ∼30 K seen in the zero magnetic

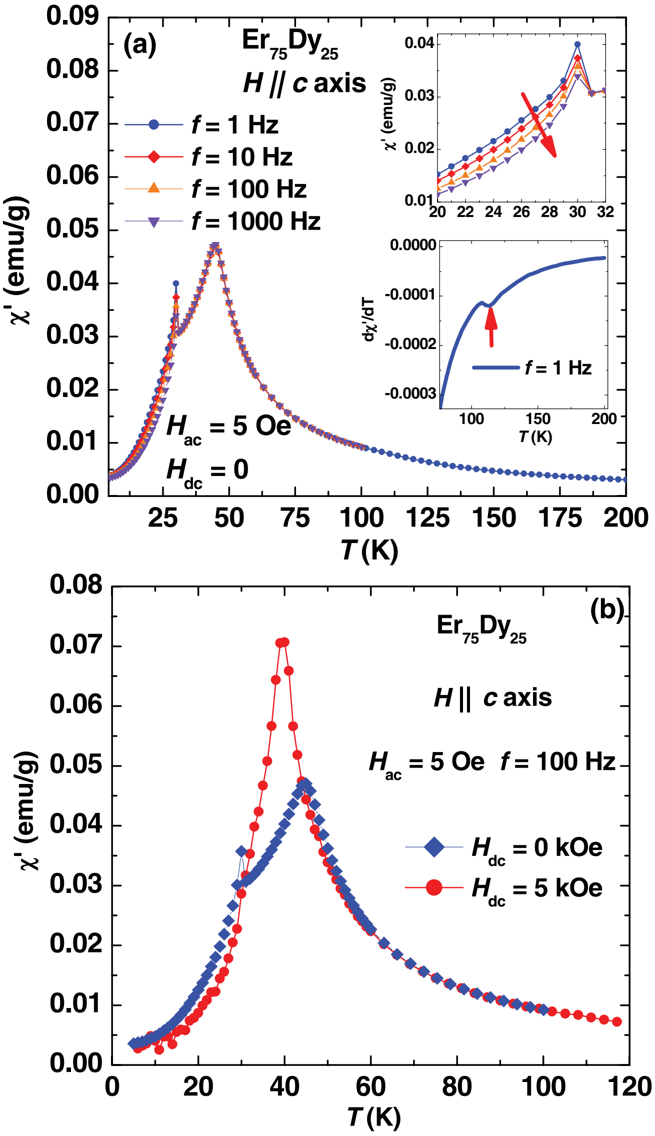

FIG. 5. (Color online) (a) The $\chi'(T)$ of $Er_{75}Dy_{25}$ measured along the *c* axis in an AC field of 5 Oe and frequencies from 1 to 1000 Hz. The upper inset shows the χ' data in the vicinity of the transition at 30 K. The lower inset shows the derivative of the 1 Hz frequency χ' data. (b) The $\chi'(T)$ of $Er_{75}Dy_{25}$ measured in DC magnetic fields of 0 and 5 kOe applied along the *c* axis in an AC field of 5 Oe and frequency of 100 Hz.

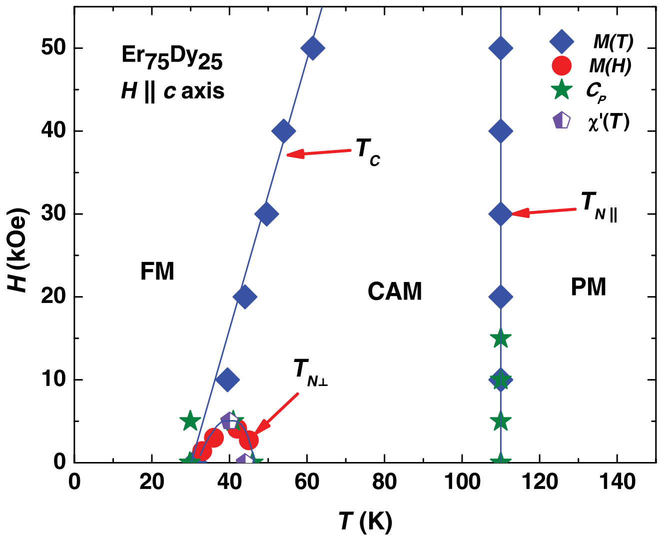

FIG. 6. (Color online) The *H*-*T* phase diagram of the $Er_{75}Dy_{25}$ single crystal for applied magnetic fields along the *c* axis constructed from the data points obtained from magnetization, AC susceptibility, and C_P measurements.

field data disappears as the 5 kOe magnetic field is applied, while the peak at ∼45 K shifts to a lower temperature. The magnitude of the 45 K peak is also enhanced when the 5 kOe field is applied.

The *H*-*T* phase diagram of the $Er_{75}Dy_{25}$ single crystal with the magnetic field applied along the *c* axis, which was constructed using data from Figs. 1–5, is shown in Fig. 6. Above $T_{N\parallel}$, which remains unchanged with the varying magnetic field, the *c* axis moments are PM. $T_{N\perp}$, on the other hand, shows complex behavior as a function of magnetic field, while T_C increases with increasing magnetic field. Below T_C, the $Er_{75}Dy_{25}$ single crystal is FM along the *c* axis, and between T_C and $T_{N\parallel}$, it belongs to the CAM phase. A fourth phase is observed below $T_{N\perp}$, but it only exists as a small region in low magnetic fields.

B. Properties in the [10$\bar{1}$0] direction (or along the *a* axis)

Figure 7 shows the C_P of $Er_{75}Dy_{25}$ measured at different magnetic fields applied parallel to the *a* axis. The sharp, first-order peak is still observed in a 15 kOe field applied along the *a* axis, while it was completely suppressed by the same field applied along the *c* axis (see Fig. 1(b)). The insets of Fig. 7(a) and (b) show the C_P data in the vicinity of the ∼45 and ∼110 K transitions, respectively. The 45 K anomaly shifts to a higher temperature region with an increasing magnetic field applied along the *a* axis, while it shifts to a lower temperature when the field is applied along the *c* axis (see Fig. 1(b)). As shown

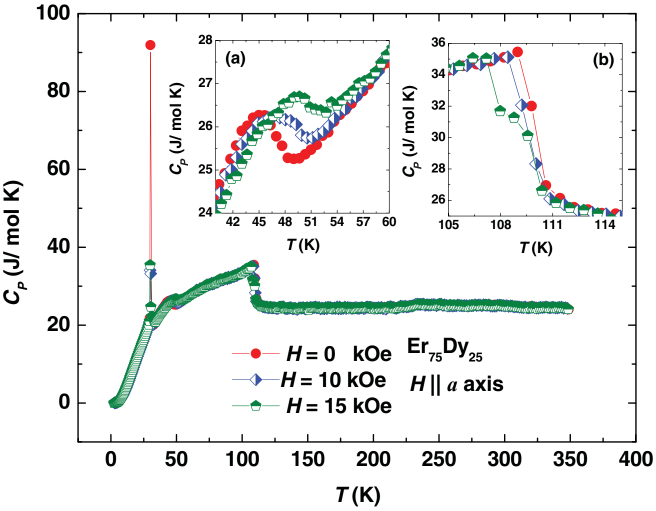

FIG. 7. (Color online) The C_P of the $Er_{75}Dy_{25}$ single crystal as a function of temperature measured at different magnetic fields applied along the *a* axis. (a) The region near the 45 K anomaly. (b) The region near the 110 K anomaly.

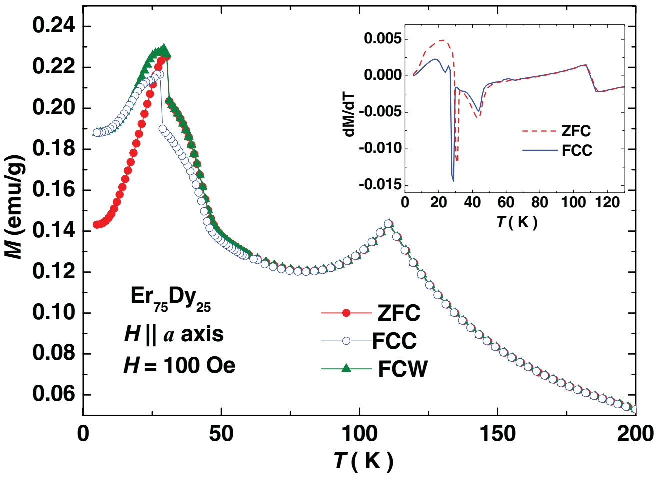

FIG. 8. (Color online) The $M(T)$ of $Er_{75}Dy_{25}$ measured in a field of 100 Oe applied along the a axis under ZFC, FCC, and FCW conditions. The inset shows the derivatives of the ZFC and FCC data.

in the inset of Fig. 7(b), the ∼110 K transition shifts to lower temperatures as the magnetic field increases.

All transitions observed in the C_P and c axis $M(T)$ data are clearly observed in the a axis $M(T)$ data measured in the 100 Oe magnetic field, as shown in Fig. 8. However, the nature of the $M(T)$ data along the a axis is quite different from that of the $M(T)$ data along the c axis. This difference is due to the a axis being the hard magnetization direction. The 110 K anomaly, which is weak and only observed in the derivative of the $M(T)$ data along the c axis, is clearly seen as AFM ordering in the $M(T)$ along the a axis. The APD-CAM transition is also observed in the derivative of the $M(T)$ data at $T_{N\perp} \cong 42$ K, as shown in the inset of Fig. 8.

Figure 9 shows the $M(T)$ data along the a axis of $Er_{75}Dy_{25}$ measured in magnetic fields ranging from 10 to 50 kOe. A sharp increase in magnetization is observed when the magnetic field is increased from 20 to 30 kOe. Similar to the magnetization of pure Er,[5] this is most likely due to the field-induced transition from an FM cone to an FM fan structure. A fourth transition is observed below T_C that shifts to a lower temperature when the magnetic field is increased and eventually disappears when the field reaches 50 kOe. This transition is more clearly observed in the derivative of the $M(T)$ data, as shown in the inset of Fig. 9, where the transition temperature is marked as T_4.

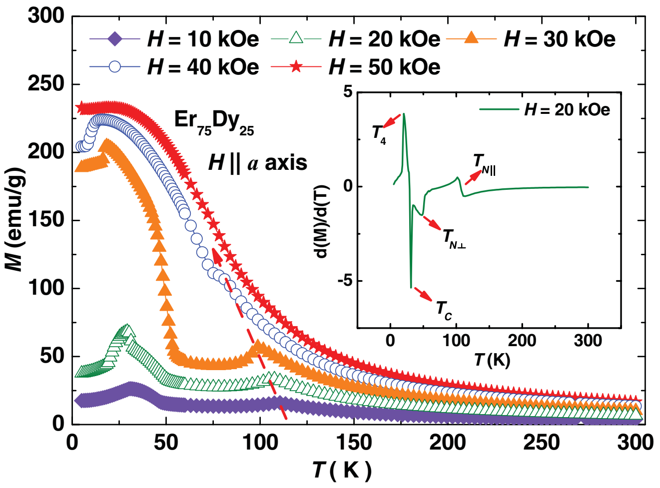

FIG. 9. (Color online) The $M(T)$ of $Er_{75}Dy_{25}$ measured in different magnetic fields from 10 to 50 kOe in 10 kOe increments applied along the a axis. The inset shows the derivative of the $M(T)$ data obtained at 20 kOe.

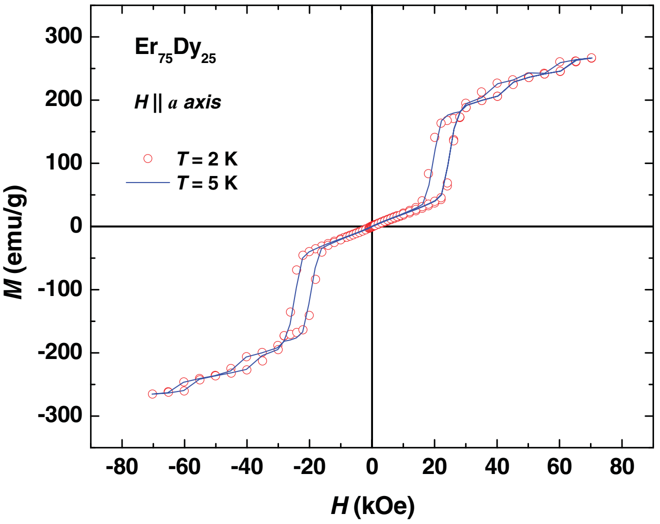

FIG. 10. (Color online) The field dependence of magnetization along the a axis of $Er_{75}Dy_{25}$ measured at 2 and 5 K.

The 2 and 5 K isothermal magnetization data of $Er_{75}Dy_{25}$ measured with the magnetic field applied along the a axis are shown in Fig. 10. The metamagnetic nature of the magnetization data is clear in the figure. A sharp increase of magnetization starts at a critical magnetic field, $H_C \cong 22$ kOe, which is consistent with the $M(T)$ data shown in Fig. 9. The metamagnetic transition represents the field-induced transformation from an FM cone phase to an FM fan phase, which is observed in pure Er when the field is applied along the a and b axes. Above ∼28 kOe, several steplike increases in magnetization are probably related to the fourth transition that is observed below T_C in Fig. 9. Hysteresis is observed in the magnetization data in the vicinity of 22, 28, and 60 kOe. At a magnetic field of 70 kOe, the moment is ∼267 emu/g (7.93 μ_B) and does not saturate.

As shown in Fig. 11, magnetic field-induced metamagnetic transitions from the FM cone to the FM fan are observed below 100 K. Above 100 K, the magnetization data exhibit PM behavior. Additional steps of magnetization observed in the 2 and 5 K data (see Fig. 10) are not seen at 15 K and higher temperatures.

The $\chi'(T)$ data measured along the a axis of the $Er_{75}Dy_{25}$ single crystal at several frequencies are shown in Fig. 12. As seen here, there is no frequency dependence of the $\chi'(T)$ data. The behavior of the $\chi'(T)$ data is similar to that of the 100 Oe $M(T)$ data shown in Fig. 8. All transitions observed in the 100 Oe $M(T)$ DC data are observed in the $\chi'(T)$ AC magnetic susceptibility data. The derivative of the $\chi'(T)$ data, shown in the inset of Fig. 12, also compares well with the derivative of the $M(T)$ data, shown in Fig. 10. This was not the case with the measurements along the c axis of $Er_{75}Dy_{25}$, where the behavior of the $M(T)$ and $\chi'(T)$ data were quite different (see Figs. 2 and 5).

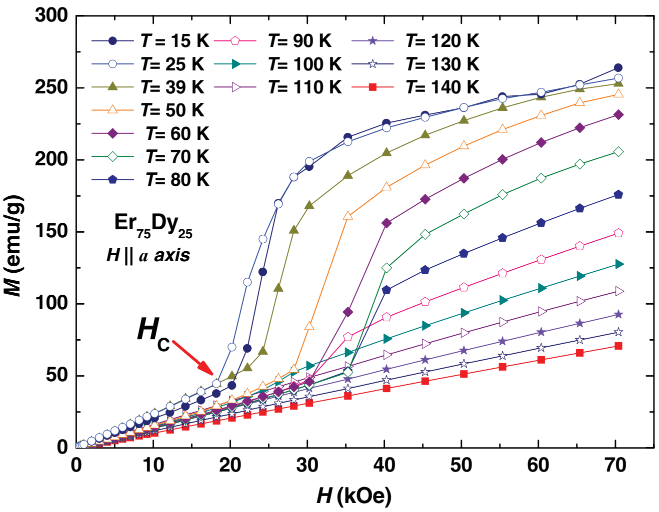

FIG. 11. (Color online) The field dependence of magnetization along the *a* axis of $Er_{75}Dy_{25}$ measured at different temperatures.

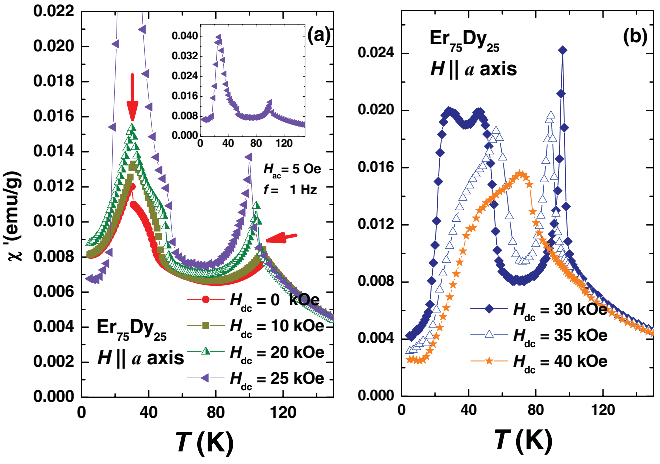

FIG. 13. (Color online) The $\chi'(T)$ of $Er_{75}Dy_{25}$ measured in DC magnetic fields of (a) 0, 10, 20, and 25 kOe (the inset shows the complete χ' data measured at 25 kOe) and (b) 30, 35, and 40 kOe, applied along the *a* axis in an AC field of 5 Oe and frequency of 1 Hz.

As shown in Fig. 13, the behavior of $\chi'(T)$ with the field applied along the *a* axis of $Er_{75}Dy_{25}$ changes significantly when bias DC magnetic fields are applied in the same direction. The peak at ∼30 K (shown by a vertical arrow in Fig. 13(a)) is strongly enhanced as the magnetic field increases. Up to 20 kOe, the enhancement of the 30 K peak is proportional to the applied magnetic field. The peak enhancement is most dramatic when a magnetic field of 25 kOe is applied (Fig. 13(a) inset). When the magnetic field exceeds 25 kOe, the peak begins to diminish. The peak at 110 K (shown by a tilted arrow in Fig. 13(a)) both sharpens and shifts to lower temperature with an increasing magnetic field up to 30 kOe. At 35 kOe the peak value of χ' diminishes, and at 40 kOe the 110 K anomaly is no longer visible (Fig. 13(b)).

The *H*-*T* phase diagram of the $Er_{75}Dy_{25}$ single crystal along the *a* axis is shown in Fig. 14. The phase diagram along the *a* axis is significantly different and more complex than the phase diagram along the *c* axis (see Fig. 6). The transition temperatures show strong dependence on the applied magnetic field. T_C remains ∼30 K until the field reaches ∼20 kOe, above which T_C increases with the increasing magnetic field. The H_C obtained from the $M(H)$ data initially remains same up to ∼30 K and then increases with increasing temperature. The ∼45 K anomaly representing the APD-CAM transition shifts to higher temperatures as the field is increased, while the ∼110 K anomaly that represents the CAM-PM transformation shifts to lower temperatures with increasing field. The two transitions merge at ∼70 K and ∼40 kOe. As labeled in Fig. 14, below H_C the FM cone phase is dominant along the *a* axis of the $Er_{75}Dy_{25}$ single crystal. Between ∼30 and ∼50 K and below H_C, the APD phase is dominant. The CAM phase dominates between ∼50 and ∼110 K and below

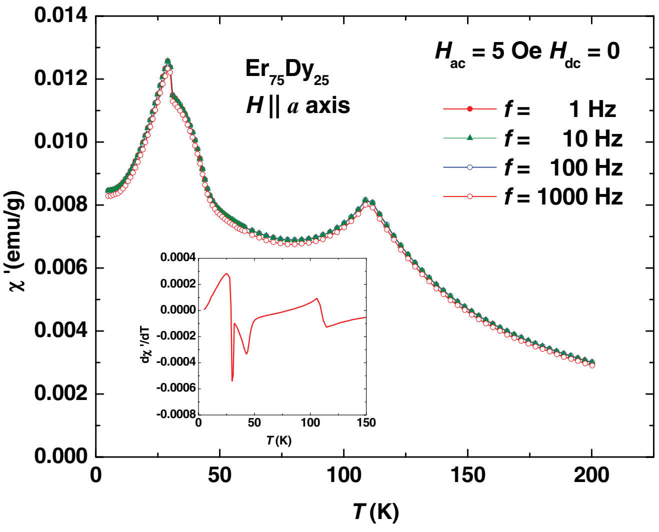

FIG. 12. (Color online) The $\chi'(T)$ of $Er_{75}Dy_{25}$ measured along the *a* axis in an AC field of 5 Oe and frequencies from 1 to 1000 Hz. The inset shows the derivative of the 1 Hz frequency χ' data.

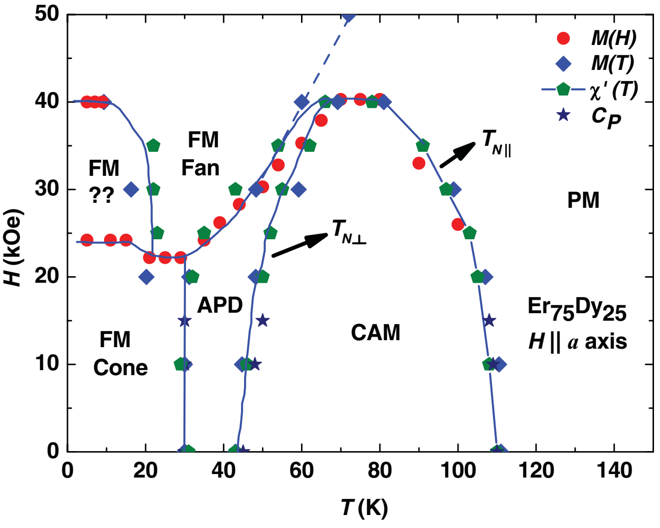

FIG. 14. (Color online) The *H*-*T* phase diagram of the $Er_{75}Dy_{25}$ single crystal for applied magnetic fields applied along the *a* axis constructed from the data points obtained from C_P, magnetization, and AC susceptibility measurements.

H_C. Above 110 K, the PM phase is dominant. Above H_C and between 10 and 60 K, the FM fan phase is stable. Below 20 K and above H_C (the region labeled as "FM ??" in Fig. 14), the phase is still FM-like but its nature is unclear.

The *H-T* phase diagram of the $Er_{75}Dy_{25}$ single crystal along the *a* axis has some similarities with the *a* axis phase diagram of the Er single crystal.[5] Magnetic phases similar to the FM, FM fan, APD, and CAM phases observed in pure Er are also observed in the $Er_{75}Dy_{25}$ single crystal. However, in pure Er, $T_{N\parallel}$ does not change with the magnetic field, while along the *a* axis of $Er_{75}Dy_{25}$, $T_{N\parallel}$ decreases with increasing magnetic field. Also, $T_{N\perp}$ decreases with increasing magnetic field along the *a* axis of the Er single crystal, while in the $Er_{75}Dy_{25}$ single crystal, the behavior of $T_{N\perp}$ is opposite. These differences in the *H-T* phase diagram of the $Er_{75}Dy_{25}$ and Er single crystals can be attributed to the addition of Dy in the $Er_{75}Dy_{25}$ single crystal. Since the easy magnetization directions and the *4f* charge densities of Dy and Er are different from one another, mixing these two elements result in the observed magnetic structures shown in Fig. 14.

Finally, the sharp peak in the C_P data and the corresponding thermal hystereses observed in the $M(T)$ data of the $Er_{75}Dy_{25}$ single crystal strongly suggest that the 30 K anomaly represents a first-order transition. It is unclear whether a structural transition is associated with this first-order transition. Since Dy undergoes a structural transition at T_C, it is possible that a structural change may be associated with the first-order transition in the $Er_{75}Dy_{25}$ single crystal. To confirm the existence of a structural transition in $Er_{75}Dy_{25}$, we plan to perform temperature dependent x-ray diffraction measurements in the future.

IV. CONCLUSIONS

Experimental investigations of the $Er_{75}Dy_{25}$ single crystal show that the *c* axis is the easy magnetization direction. Along the *c* axis, three temperature driven phase transitions are observed. A first-order FM transition is observed at $T_C \cong 30$ K, followed by two AFM transitions at ~45 and ~110 K. The first-order transformation is revealed as a sharp peak in the C_P data. The application of magnetic fields along the *c* axis suppresses the sharp peak, which disappears when the field reaches 15 kOe. The 45 K transition also disappears as the magnetic field is applied along the *c* axis. The transitions shift to either lower or higher temperatures when magnetic fields are applied along the *a* axis of the $Er_{75}Dy_{25}$ single crystal. A field-induced metamagnetic transition from the FM cone to the FM fan phase is also observed along the *a* axis. The multiple spin slip transitions that are observed in pure Er single crystals are not observed in the $Er_{75}Dy_{25}$ single crystal. The *H-T* phase diagrams along the *c* and *a* axes are significantly different: the phase diagram along the *c* axis shows the existence of FM, APD, CAM, and PM phases, while the phase diagram along the *a* axis shows that the $Er_{75}Dy_{25}$ single crystal exhibits the FM cone, the FM fan, an unknown FM, and APD, CAM, and PM phases.

ACKNOWLEDGMENTS

This work was supported by the US Department of Energy, Office of Basic Energy Science, Division of Materials Sciences and Engineering. The research was performed at the Ames Laboratory. The Ames Laboratory is operated for the US Department of Energy by Iowa State University under Contract No. DE-AC02-07CH11358.

---

[*] Present address: Department of Physics, University of Alberta, Edmonton, Alberta T6G 2J1, Canada.
[†] muk@ualberta.ca

[1] J. W. Cable, E. O. Wollan, W. C. Koehler, and M. K. Wilkinson, Phys. Rev. **140**, A1896 (1965).

[2] J. F. Elliott, S. Legvold, and F. H. Spedding, Phys. Rev. **94**, 1143 (1954).

[3] K. A. Gschneidner Jr., V. K. Pecharsky, and D. K. Fort, Phys. Rev. Lett. **78**, 4281 (1997).

[4] V. K. Pecharsky, K. A. Gschneidner Jr., and D. Fort, Scr. Mater. **35**, 843 (1996).

[5] B. H. Frazer, J. R. Gebhardt, and N. Ali, J. Appl. Phys. **85**, 6100 (1999).

[6] B. Watson and N. Ali, J. Phys. Condens. Matter **7**, 4713 (1995).

[7] A. S. Chernysov, A. O. Tsokol, A. M. Tishin, K. A. Gschneidner Jr., and V. K. Pecharsky, Phys. Rev. B **71**, 184410 (2005).

[8] B. J. Beaudry and K. A. Gschneidner Jr., in *Handbook on the Physics and Chemistry of Rare Earths*, edited by K. A. Gschneidner Jr. and L. Eyring (North-Holland Publishing, Amsterdam, 1978), Vol. 1, Chap. 2, p. 173.

[9] A. S. Chernyshov, Ya. Mudryk, V. K. Pecharsky, and K. A. Gschneidner Jr., Phys. Rev. B **77**, 094132 (2008).

[10] M. Atoji, Solid State Commun. **14**, 1041 (1974).

[11] M. K. Sanyal, D. Gibbs, J. Bohr, and M. Wulff, Phys. Rev. B **49**, 1079 (1994).

[12] F. J. Darnell, Phys. Rev. **132**, 1098 (1963).

[13] D. Gibbs, J. Bohr, J. D. Axe, D. E. Moncton, and K. L. D'Amico, Phys. Rev. B **34**, 8182 (1986).

[14] J. Jensen and A. R. Mackintosh, *Rare Earth Magnetism: Structure and Excitations* (Clarendon Press, Oxford, 1991).

[15] K. A. McEwen, in *Handbook on the Physics and Chemistry of Rare Earths*, edited by K. A. Gschneidner Jr. and L. Eyring (North-Holland, Amsterdam, 1978), Vol. 1, Chap. 6, p. 411.

[16] R. Hertz and H. Kronmüller, J. Magn. Magn. Mater. **9**, 273 (1978).

[17] T. Izawa, K. Tajima, Y. Yamamoto, M. Fujii, O. Fujimaru, and Y. Shinoda, J. Phys. Soc. Jpn. **65**, 2640 (1996).

[18] F. J. Darnell and E. P. Moore, J. Appl. Phys. **34**, 1337 (1963).

[19] F. J. Darnell, Phys. Rev. **130**, 1825 (1963).

[20] V. V. Vorob'ev, M. Ya. Krupotkin, and V. A. Finkel, Sov. Phys. JETP **61**, 1056 (1985).

[21] H. Fujii, Y. Hashimoto, T. Okamoto, N. Achiwa, and S. Kawano, J. Phys. Soc. Jpn. **50**, 2939 (1981).

[22] H. Fujii, Y. Hashimoto, and T. Okamoto, J. Phys. Soc. Jpn. **49**, 1740 (1980).

[23] D. Chatterjee and K. N. R. Taylor, J. Phys. F Met. Phys. **2**, 151 (1972).

[24] K. A. Gschneidner Jr., A. O. Pecharsky, and V. K. Pecharsky, in *Cryoolers 11*, edited by R. S. Ross Jr. (Kluwer Academic/Plenum, New York, 2001), p. 433.

[25] Y. L. Wu, A. O. Pecharsky, V. K. Pecharsky, and K. A. Gschneidner Jr., Adv. Cryog. Eng. **48**, 3 (2002).

[26] K. A. Gschneidner Jr., A. O. Pecharsky, Y. L. Wu, and V. K. Pecharsky, J. Solid State Chem. **171**, 324 (2003).

[27] A. L. Lima, K. A. Gschneidner Jr., V. K. Pecharsky, and A. O. Pecharsky, Phys. Rev. B **68**, 134409 (2003).

[28] R. Nirmala, Ya. Mudryk, V. K. Pecharsky, and K. A. Gschneidner Jr., Phys. Rev. B **76**, 014407 (2007).

[29] M. Khan, K. A. Gschneidner Jr., and V. K. Pecharsky, Phys. Rev. B **80**, 224408 (2009).

[30] M. Khan, Ya. Mudryk, D. Paudyal, K. A. Gschneidner Jr., and V. K. Pecharsky, Phys. Rev. B **82**, 064421 (2010).

[31] Materials Preparation Center, The Ames Laboratory, US Department of Energy, Ames, IA, USA [http://www.mpc.ameslab.gov].

[32] V. K. Pecharsky, J. O. Moorman, and K. A. Gschneidner Jr., Rev. Sci. Instrum. **68**, 4196 (1997).

[33] R. E. Skochdopole, M. Griffel, and F. H. Spedding, J. Chem. Phys. **23**, 2258 (1955).

[34] V. K. Pecharsky, K. A. Gschneidner Jr., and D. Fort, Phys. Rev. B **47**, 5063 (1993).

[35] R. W. Green, S. Legvold, and F. H. Spedding, Phys. Rev. **122**, 827 (1961).